Paleo-Asian oceanic slab under the North China craton revealed by carbonatites derived from subducted limestones

Item Type	Article
Authors	Chen, Chunfei; Liu, Yongsheng; Foley, Stephen F.; Ducea, Mihai N.; He, Detao; Hu, Zhaochu; Chen, Wei; Zong, Keqing
Citation	Paleo-Asian oceanic slab under the North China craton revealed by carbonatites derived from subducted limestones 2016, 44 (12):1039 Geology
DOI	10.1130/G38365.1
Publisher	GEOLOGICAL SOC AMER, INC
Journal	Geology
Rights	© Geological Society of America.
Download date	26/08/2022 05:15:29
Item License	http://rightsstatements.org/vocab/InC/1.0/
Version	Final accepted manuscript
Link to Item	http://hdl.handle.net/10150/622796

Paleo-Asian Oceanic slab under the North China Craton revealed by carbonatites derived from subducted limestones

Chunfei Chen[1], Yongsheng Liu[1*], Stephen F. Foley[2], Mihai N. Ducea[3,4], Detao He[1],

Zhaochu Hu[1], Wei Chen[1], and Keqing Zong[1]

[1]State Key Laboratory of Geological Processes and Mineral Resources, School of Earth

Sciences, China University of Geosciences, Wuhan 430074, China

[2]ARC Centre of Excellence for Core to Crust Fluid Systems, Dept. of Earth and Planetary

Sciences, Macquarie University, North Ryde, New South Wales 2109, Australia

[3]Department of Geosciences, University of Arizona, Tucson, Arizona 85721, USA

[4]Faculty of Geology and Geophysics, University of Bucharest, Bucharest, Romania

*E-mail: yshliu@hotmail.com

ABSTRACT

It is widely accepted that the lithospheric mantle under the North China Craton

(NCC) has experienced comprehensive refertilization due to input from surrounding

subducted slabs. However, the possible contribution from the Paleo-Asian Oceanic slab

from the north is poorly constrained, largely because of the lack of convincing evidence for

the existence of this slab under the NCC. We report here carbonatite intruding into

Neogene alkali basalts in the Hannuoba region, close to the northern margin of the NCC.

Trace element patterns with positive Sr and U anomalies, negative HFSE (Nb, Ta, Zr, Hf

and Ti) and Ce anomalies, high $^{87}Sr/^{86}Sr$ ratios (0.70522-0.70796) and high $\delta^{18}O_{SMOW}$

values (22.2–23‰) indicate that this carbonatite had a limestone precursor. However, the

presence of coarse-grained mantle-derived clinopyroxene, orthopyroxene and olivine, and

chemical features of the carbonates suggest that the carbonate melts were derived from the

mantle. The carbonates have high $^{143}Nd/^{144}Nd$ ratios (0.51282–0.51298) and show

negative correlation between CaO and Ni contents, resulting from reaction between

carbonate melt and peridotite. Considering the regional tectonic setting, the carbonatite

probably formed by melting of subducted sedimentary carbonate rocks that formed part of

the Paleo-Asian Oceanic slab, thus could provide the first direct evidence for the presence

of the Paleo-Asian Oceanic slab beneath the NCC.

INTRODUCTION

Carbonate platforms occur quite commonly in oceanic realms. Small tropical

oceans, exemplified by many segments of the Tethyan ocean in Europe, were covered with

extensive carbonate platforms, found today in classic Alpine fold and thrust belts. Clearly,

some of these materials are subducted to mantle depths where they undergo decarbonation

reactions and may be involved in partial melting (Collins et al., 2015; Doucelance et al.,

2014; Ducea et al., 2005; Hammouda, 2003). Enormous budgets of CO_2 at magmatic arcs

(Lee and Lackey, 2015) independently require that carbonate is a major player in mass

exchange at convergent margins. Subduction magmatism is probably one of the most

important tectonic mechanisms responsible for regulating the exchange of CO_2 between

the Earth's interior and the atmosphere (McKenzie et al., 2016). Unfortunately, very little

observational data exist to provide details on the mechanisms of transport of carbonate

materials and CO_2 from the surface to mantle depths and back to the Earth's surface via

fluid (decarbonation reactions) and melt transport (Liu et al., 2015).

It has been suggested that the lithosphere of the North China Craton (NCC) was

successively modified by (1) the southward subduction of the Paleo-Asian oceanic slab

(PAOS) between the early Paleozoic and the late Permian, (2) the northward subduction of

the Paleo-Tethyan oceanic and Yangtze plates in the Triassic and (3) the westward

subduction of the Pacific plate since the Cretaceous (Fig. 1A) (Windley et al., 2010).

Although all of these subduction events could have contributed to widespread lithospheric

reactivation and thinning under the NCC (e.g., Griffin et al., 1998), the Pacific plate

subduction was generally advocated to account for the lithospheric thinning (Zhu et al.,

2011). The contribution of the PAOS and Paleo-Tethyan oceanic slab to lithospheric

thinning remains enigmatic, largely because of the lack of convincing evidence for the

existence of these slabs under the NCC. If abundant carbonate sediments were transported

into deep mantle during oceanic slab subduction, they could have contributed

fundamentally to the modification of the chemical and physical properties of the

lithospheric mantle by carbonate metasomatism. In turn, subsequent mantle-derived melts

(especially carbonatite) could contain the fingerprint of subducted carbonate, which can be

used to trace the origin of the subducted slab (Tappert et al., 2009) and outline the

crust-mantle recycling of carbonate sediments.

Here, we document a carbonatite intrusion with geochemical features of recycled limestone. The intrusion marks the subduction of an overlying carbonate platform of the PAOS, to mantle depths beneath the NCC, providing evidence for recycling of carbonate back to the Earth's surface by buoyant diapirism and high-degree melting.

SAMPLES, PETROLOGY, AND GEOCHEMICAL COMPOSITIONS

Samples were collected from a carbonatite intrusion (0.5–3 m thick and >35 m wide) which intrudes into Neogene basalts (10–22 Ma; Zhu (1998)) at Hannuoba (Fig. 1). The basalts are distributed along the northern margin of the NCC, and comprise intercalated tholeiitic, transitional and alkali basalts (Zhi et al., 1990). The source of the basalts probably contains abundant garnet-pyroxenite (Liu et al., 2008) or was metasomatized by carbonate-rich fluid (Dupuy et al., 1992). The alkali basalts carry abundant granulite, pyroxenite and peridotite xenoliths (Chen et al., 2001). The evolved Sr-Nd isotopic compositions of some pyroxenite xenoliths indicate involvement of subducted sediments (e.g., Xu, 2002). The carbonatite intrusion occurs in xenolith-free basalt and has a sharp boundary with the basalt layer. The overlying basalt is domed upwards by the invasion of the carbonatite melt (Fig. 1B).

The carbonatite contains aggregates of calcite phenocrysts and medium- to coarse-grained silicate macrocrysts set in a matrix of fine-gained calcite (Fig. 1C-D) indicating rapid quenching. Monomineralic aggregates of interlocking calcite grains (50–100 μm) indicate calcite accumulation before quenching. The silicate macrocrysts

consist of coarse-grained clinopyroxene (Cpx, 0–15 vol.%), orthopyroxene (Opx, 0–12

vol.%), olivine (Ol, 0–10 vol.%) and rare spinel (Sp, 0–1.5 vol.%). Ol is forsteritic (Fo =

90–91) and has low CaO contents (<0.1 wt.%) but high Ni contents (2809–3062 ppm), and

Opx and Cpx have Mg# values of 90.8–91.6 and 91.9–93.3 respectively (Table DR1).

Many macrocrysts consist of recrystallized pseudomorphs of calcite replacing the silicate

minerals, indicating resorption in the carbonate melt (Fig. 1C). Moissanite (20–80μm),

highly disordered graphite (10–30μm) and Na-K chlorides (~20μm) were found (Figure

DR1). Moissanite was identified by characteristic Raman peaks at 769, 791 and 970 cm^{-1}

and highly disordered graphite was identified by Raman bands at 1358 cm^{-1} and 1589 cm^{-1}

(Figure DR1).

Whole-rock compositions of the carbonatites have high CaO (44.1–53.9 wt.%),

intermediate MgO (0.8–4.8 wt.%) and low alkali contents (Na_2O <0.01 wt.% and K_2O

<0.05 wt.%); many are similar to limestones, and some lie along a mixing trend between

limestone and peridotite (Figure DR2). MgO contents in the carbonatites are higher than in

limestones (0.13–1.65 wt.%), and show a negative correlation with CaO. Trace element

patterns are similar to sedimentary limestones with notably positive Sr and U anomalies

and negative high field strength elements (HFSE: Zr, Hf, Nb, Ta, Ti) anomalies (Fig. 2).

The incompatible trace element contents of most samples are lower than average

limestone, especially for Rb, Ba and heavy rare earth elements (REE) (Fig. 2). Their REE

patterns show negative Ce anomalies (Ce/Ce* = 0.2–0.8) and positive Eu anomalies

(Eu/Eu* = 1.15–2.98) (Table DR2). The carbonate matrix contains 45.2–52.7 wt.% CaO,

0.4–1.8 wt.% MgO and 1.5–5.0 wt.% SiO_2 (Table DR3). Both the carbonate matrix and

phenocrysts have higher Ni contents (1–133 ppm) than limestone, and show negative

correlations between CaO and Ni (Fig. 3A).

Carbonates in the carbonatite intrusion have higher $^{87}Sr/^{86}Sr$ (0.70522–0.70796)

and slightly higher $^{143}Nd/^{144}Nd$ (0.51282–0.51298) than typical carbonatites (Fig. 3B).

$^{143}Nd/^{144}Nd$ ratios show no correlation with Nd contents (0.4–2.8 ppm), whereas $^{87}Sr/^{86}Sr$

ratios correlate negatively with Sr contents (27–306 ppm) (Figure DR3). Rare aragonite

veinlets which crosscut one sample possess high Sr contents (2507–6600 ppm) and

relatively low $^{87}Sr/^{86}Sr$ ratios (0.70411–0.70683) (Table DR4): the post-magmatic fluid

that deposited this aragonite might have also partially modified the sample (Fig. 3B). The

primary carbonatitic melts represented by the low-Sr samples have the highest $^{87}Sr/^{86}Sr$

and $^{143}Nd/^{144}Nd$ ratios. The carbonatites are characterized by light carbon isotopic

compositions ($\delta^{13}C_{VPDB}$ = -14.4‰ to -11.2‰) but heavy oxygen isotopic compositions

($\delta^{18}O_{SMOW}$ = 22.2‰ to 23‰) (Table DR2).

DISCUSSION

Mantle Derivation of the Carbonatite

Possible origins of the Ol and Cpx macrocrysts in the carbonatite intrusion are

reaction products between carbonate melt and the basalt wallrock (Jolis et al., 2013) or

peridotite xenocrysts from the mantle that potentially provide records of the ascent process

of the carbonatite melts. The compositions of Ol (CaO <0.1 wt.%) and Cpx (Mg# = 91.9–93.3 and SiO_2 >50.1 wt.%) macrocrysts clearly correspond to minerals in mantle peridotites and are unlike products of carbonate melt-basalt interaction (Figure DR4). This conclusion is supported by the Ni contents of Opx and Cpx (Table DR1), which are also typical for mantle minerals (Foley et al., 2006). Ol produced by carbonate melt-basalt interaction would have higher CaO (>1.31 wt.%), and Cpx would be characterized by low Mg# (<84) and low SiO_2 content (<45 wt.%) (Jolis et al., 2013). The temperatures estimated from Cpx+Opx macrocryst pairs are 770–932 ºC (see supplementary information), implying a source depth of ~50 km for the disrupted mantle xenoliths on the documented geotherm for the northern margin of the NCC (Chen et al., 2001). Hydrous carbonatitic liquids are known to occur at temperatures as low as 870-900 ºC (Poli, 2015), at the upper end of this temperature range. Furthermore, highly disordered graphite found in the Hannuoba carbonatite intrusion might be the result of the transformation of diamond during rapid upward migration from the deeper mantle, as suggested by diamond-bearing carbonatite xenoliths (Liu et al., 2015). High Ni contents and high $^{143}Nd/^{144}Nd$ ratios of carbonate components in the carbonatite intrusion indicate that interaction between the carbonate melt and peridotite occurred (Fig. 3), as also demonstrated by resorption of olivine macrocrysts in the carbonatite melt (Fig. 1C). In combination, these observations indicate that the carbonatite melt originated at mantle depths, or at least resided long enough in the mantle to acquire these compositional characteristics.

Subducted Sedimentary Carbonate Precursor for the Carbonatite

Mantle-derived carbonatites typically exhibit enriched incompatible trace element contents (e.g., LREE, Nb, Sr and Ba) and steep LREE-enriched patterns (Jones et al., 2013). Contrasting with this, the Hannuoba carbonatites have much lower trace element contents, and show trace element patterns similar to limestone (Fig. 2). Furthermore, they have high $\delta^{18}O_{SMOW}$ values (22.2–23‰), high $^{87}Sr/^{86}Sr$ ratios (0.70522-0.70796) (Fig. 3B), trace element patterns with positive Sr and U anomalies and negative HFSE and Ce anomalies (Fig. 2), all of which are typical features of sedimentary limestones (Jin et al., 2009). In the CaO-MgO-SiO$_2$ plot, they form a trend consistent with interaction between pure limestone and peridotite (Figure DR2): their $^{87}Sr/^{86}Sr$ and $^{143}Nd/^{144}Nd$ ratios and high Ni contents can be modeled by simple mixing between limestone and peridotite (Fig. 3). Taken together, these features suggest the carbonatite intrusion formed from melts of subducted limestone, which interacted with peridotite at depths of at least 50 km and possibly 150 km, incorporating peridotite minerals as xenocrysts.

The incompatible trace elements, especially those highly mobilized in aqueous fluids (e.g., Rb and Ba), have lower concentrations in the Hannuoba carbonatites than in average limestone (Fig. 2), indicating that the subducted limestone precursor could have been partially modified by aqueous fluids in the subduction zone. Furthermore, the much lower HREE contents and positive Eu anomalies in the carbonatites compared to average limestone (Fig. 2) might be attributed to modification by subduction-related CO_3^{2-}-rich

aqueous fluids. $HREE^{3+}$ are complexed more strongly by CO_3^{2-} than $LREE^{3+}$ and similarly

$LREE^{3+}$ are complexed more strongly by CO_3^{2-} than Eu^{2+} (Bau, 1991), so that $HREE^{3+}$

would be removed easily from limestone by a CO_3^{2-}-rich fluid, but Eu^{2+} could be retained.

Melting of limestone is commonly regarded to be restricted to unusually hot

regimes (Wyllie and Tuttle, 1960), although the temperatures involved may be reduced in

water-bearing conditions (Poli, 2015). Due to the high solidus temperatures but lower

density and viscosity, limestone cannot be melted at the top of the subducted slab, but may

penetrate into the cold cratonic mantle in the form of solid buoyant diapirs (Behn et al.,

2011). The large scale of basalts in the Hannuoba area (~1700 km^2) indicates a giant

Cenozoic thermal event in the mantle under the northern margin of the NCC, which could

have resulted in substantial melting of such limestone diapirs. Limestone is mostly

composed of a single calcite phase, so it is reasonable to speculate that high modes of

melting of subducted limestone would occur once melting initiates. High-degree melting

of a subducted limestone in the mantle was also suggested by Liu et al. (2015) to account

for the mantle-derived carbonatite xenoliths from the Dalihu area with the geochemical

features of limestone. The Hannuoba carbonatite intrusion may share a similar origin to the

carbonatite xenoliths reported by Liu et al. (2015), but were emplaced into the shallow

crust. The carbonatite melt might have experienced complex devolatilization during ascent

(Russell et al., 2012), which could have produced the low $\delta^{13}C_{VPDB}$ values of carbonatite

melt (Cartigny et al., 1998) and also yielded extremely local, strongly reducing conditions

that permitted the formation of moissanite (Shiryaev and Gaillard, 2014). This would

explain both the much lower $\delta^{13}C_{VPDB}$ values of the Hannuoba carbonatites relative to

average limestone ($-0.44 \pm 2‰$, (1σ, n = 102)), and the occurrence of moissanites in the

Hannuoba intrusion (Figure DR1).

Implications for the Subduction of the Paleo-Asian Oceanic Slab under the NCC

The $^{87}Sr/^{86}Sr$ ratios of sedimentary carbonate rocks have varied with time (Veizer et

al., 1999) (Figure DR5), so that the high Sr isotopic compositions can be used to constrain

the age of the limestone. $^{87}Sr/^{86}Sr$ ratios of marine carbonates increased from ≤ 0.702 in the

Archaean to ~0.7069 in the late Neoproterozoic, and then varied within a small range

(0.7069–0.7089) during the Phanerozoic. The highest $^{87}Sr/^{86}Sr$ ratio (0.70791) of carbonate

in the Hannuoba carbonatite represents materials least contaminated by aragonite veins and

mantle materials (Fig. 3B), inferring that the age of the limestone source of the carbonatite

is most probably between 360 and 580 Ma, and certainly not older than 580 Ma (Figure

DR5); this is consistent with its derivation from the Paleo-Asian Ocean, which existed

between 1 Ga and 250 Ma (Xiao et al., 2003). Furthermore, the carbonatite intrusion occurs

>1000 km from the trench position of the east Pacific plate and the Qinling-Dabie-Sulu

Orogenic belt, but within 200km of the northern margin of the NCC (Fig. 1A). The Pacific

slab is eliminated as a possible source because it is stagnating in the mantle transition zone

beneath the eastern NCC (Zhao et al., 2009) at a depth to which limestone could not be

subducted due to its low density and viscosity. These observations suggest that the

limestone precursor was most probably derived from the subducted PAOS.

It is noteworthy that Mesozoic carbonatites from Zhuolu and Huairen ~50–100 km

south of Hannuoba have high $^{87}Sr/^{86}Sr$ ratios (0.7055–0.7075) (Yan et al., 2007) (Figs. 1

and 3B) similar to the Hannuoba carbonatite intrusion, implying that they may also be

related to the PAOS. Although the Mesozoic Zhuolu and Huairen carbonatites have

similarly lower trace element contents than typical carbonatite, they have much higher

trace element contents than the Cenozoic Hannuoba intrusion (Fig. 2). This suggests that

the Mesozoic carbonatites could have been derived from partial melting of subducted

carbonate-rich eclogite rather than limestone. The Hannuoba, Zhuolu and Huairen

carbonatites are distributed in a north-south direction, and show increasing trace element

contents with increasing distance from the north margin of the NCC (Figs. 2 and 4). The

temporal and spatial variations of the Mesozoic and Cenozoic carbonatites are consistent

with the interpretation that carbonated eclogite could be subducted deep into the mantle

(Hammouda, 2003) before melting, whereas limestone would detach from the downgoing

slab to form buoyant diapirs penetrating into the shallow and cold mantle (Behn et al.,

2011; Liu et al., 2015) (Fig. 4). Subsequently, a giant Cenozoic mantle thermal event, as

indicated by the large-scale Hannuoba basalts, triggered high-degree melting of the

limestones, now in the shallower mantle. These carbonatites reconstruct the path of the

consumed PAOS under the NCC, which is critical for understanding how subduction zones

modulate the global carbon cycle.

ACKNOWLEDGMENTS

REFERENCES CITED

Bau, M., 1991, Rare-earth element mobility during hydrothermal and metamorphic

fluid-rock interaction and the significance of the oxidation state of europium:

Chemical Geology, v. 93, p. 219–230, doi:10.1016/0009-2541(91)90115-8.

Behn, M.D., Kelemen, P.B., Hirth, G., Hacker, B.R., and Massonne, H.-J., 2011, Diapirs as

the source of the sediment signature in arc lavas: Nature Geoscience, v. 4, p. 641–646,

doi:10.1038/ngeo1214.

Cartigny, P., Harris, J.W., and Javoy, M., 1998, Eclogitic Diamond Formation at Jwaneng:

No Room for a Recycled Component: Science, v. 280, p. 1421–1424,

doi:10.1126/science.280.5368.1421.

Chen, S.H., O'Reilly, S.Y., Zhou, X.H., Griffin, W.L., Zhang, G.H., Sun, M., Feng, J.L.,

and Zhang, M., 2001, Thermal and petrological structure of the lithosphere beneath

Hannuoba, Sino-Korean Craton, China: Evidence from xenoliths: Lithos, v. 56,

p. 267–301, doi:10.1016/S0024-4937(00)00065-7.

Collins, N.C., Bebout, G.E., Angiboust, S., Agard, P., Scambelluri, M., Crispini, L., and

John, T., 2015, Subduction zone metamorphic pathway for deep carbon cycling: II.

Evidence from HP/UHP metabasaltic rocks and ophicarbonates: Chemical Geology,

v. 412, p. 132–150, doi:10.1016/j.chemgeo.2015.06.012.

Doucelance, R., Bellot, N., Boyet, M., Hammouda, T., and Bosq, C., 2014, What coupled

cerium and neodymium isotopes tell us about the deep source of oceanic carbonatites:

Earth and Planetary Science Letters, v. 407, p. 175–186,

doi:10.1016/j.epsl.2014.09.042.

Ducea, M.N., Saleeby, J., Morrison, J., and Valencia, V.A., 2005, Subducted carbonates,

metasomatism of mantle wedges, and possible connections to diamond formation: An

example from California: The American Mineralogist, v. 90, p. 864–870,

doi:10.2138/am.2005.1670.

Dupuy, C., Liotard, J., and Dostal, J., 1992, Zr/Hf fractionation in intraplate basaltic rocks:

carbonate metasomatism in the mantle source: Geochimica et Cosmochimica Acta,

v. 56, p. 2417–2423, doi:10.1016/0016-7037(92)90198-R.

Foley, S.F., Andronikov, A.V., Jacob, D.E., and Melzer, S., 2006, Evidence from Antarctic

mantle peridotite xenoliths for changes in mineralogy, geochemistry and geothermal

gradients beneath a developing rift: Geochimica et Cosmochimica Acta, v. 70,

p. 3096–3120, doi:10.1016/j.gca.2006.03.010.

Griffin, W.L., Andi, Z., O'Reilly, S.Y., and Ryan, C.G., 1998, Phanerozoic evolution of

the lithosphere beneath the SinoKorean craton, *in* Flower, M.F.J., et al., eds., Mantle

dynamics and plate interactions in East Asia: Geodynamics Series: Washington, D.C.,

American Geophysical Union, v. 27, p. 107–126.

Hammouda, T., 2003, High-pressure melting of carbonated eclogite and experimental

constraints on carbon recycling and storage in the mantle: Earth and Planetary Science

Letters, v. 214, p. 357–368, doi:10.1016/S0012-821X(03)00361-3.

Jin, Z.J., Zhu, D.Y., Hu, W.X., Zhang, X.F., Zhang, J.T., and Song, Y.C., 2009,

Mesogenetic dissolution of the middle Ordovician limestone in the Tahe oilfield of

Tarim basin, NW China: Marine and Petroleum Geology, v. 26, p. 753–763,

doi:10.1016/j.marpetgeo.2008.08.005.

Jolis, E.M., Freda, C., Troll, V.R., Deegan, F.M., Blythe, L.S., McLeod, C.L., and

Davidson, J.P., 2013, Experimental simulation of magma–carbonate interaction

beneath Mt. Vesuvius, Italy: Contributions to Mineralogy and Petrology, v. 166,

p. 1335–1353, doi:10.1007/s00410-013-0931-0.

Jones, A.P., Genge, M., and Carmody, L., 2013, Carbonate melts and carbonatites:

Reviews in Mineralogy and Geochemistry, v. 75, p. 289–322,

doi:10.2138/rmg.2013.75.10.

Lee, C.-T.A., and Lackey, J.S., 2015, Global Continental Arc Flare-ups and Their Relation

to Long-Term Greenhouse Conditions: Elements, v. 11, p. 125–130,

doi:10.2113/gselements.11.2.125.

Liu, Y.S., Gao, S., Kelemen, P.B., and Xu, W.L., 2008, Recycled crust controls contrasting

source compositions of Mesozoic and Cenozoic basalts in the North China Craton:

Geochimica et Cosmochimica Acta, v. 72, p. 2349–2376,

doi:10.1016/j.gca.2008.02.018.

Liu, Y.S., He, D.T., Gao, C.G., Foley, S.F., Gao, S., Hu, Z.C., Zong, K.Q., and Chen, H.H.,

2015, First direct evidence of sedimentary carbonate recycling in subduction-related

xenoliths: Scientific Reports, v. 5, p. 11547, doi:10.1038/srep11547.

McDonough, W.F., and Sun, S.S., 1995, The composition of the Earth: Chemical Geology,

v. 120, p. 223–253, doi:10.1016/0009-2541(94)00140-4.

McKenzie, N.R., Horton, B.K., Loomis, S.E., Stockli, D.F., Planavsky, N.J., and Lee,

C.-T.A., 2016, Continental arc volcanism as the principal driver of

icehouse-greenhouse variability: Science, v. 352, doi:10.1126/science.aad5787.

Poli, S., 2015, Carbon mobilized at shallow deths in subduction zones by carbonatitic

liquids: Nature Geoscience, v. 8, p. 633-637, doi:10.1038/NGEO2464

Russell, J.K., Porritt, L.A., Lavallee, Y., and Dingwell, D.B., 2012, Kimberlite ascent by

assimilation-fuelled buoyancy: Nature, v. 481, p. 352–356, doi:10.1038/nature10740.

Shiryaev, A.A., and Gaillard, F., 2014, Local redox buffering by carbon at low pressures

and the formation of moissanite – natural SiC: European Journal of Mineralogy, v. 26,

p. 53–59, doi:10.1127/0935-1221/2013/0025-2339.

Tappert, R., Foden, J., Stachel, T., Muehlenbachs, K., Tappert, M., and Wills, K., 2009,

Deep mantle diamonds from South Australia: A record of Pacific subduction at the

Gondwanan margin: Geology, v. 37, p. 43–46, doi:10.1130/G25055A.1.

Veizer, J., et al., 1999, $^{87}Sr/^{86}Sr$, $\delta^{13}C$ and $\delta^{18}O$ evolution of Phanerozoic seawater:

Chemical Geology, v. 161, p. 59–88, doi:10.1016/S0009-2541(99)00081-9.

Windley, B.F., Maruyama, S., and Xiao, W.J., 2010, Delamination/thinning of

sub-continental lithospheric mantle under Eastern China: The role of water and

multiple subduction: American Journal of Science, v. 310, p. 1250–1293,

doi:10.2475/10.2010.03.

Wyllie, P.J., and Tuttle, O.F., 1960, The system CaO-CO2–H2O and the origin of

carbonatites: Journal of Petrology, v. 1, p. 1–46, doi:10.1093/petrology/1.1.1.

Xiao, W.J., Windley, B.F., Hao, J., and Zhai, M.G., 2003, Accretion leading to collision

and the Permian Solonker suture, Inner Mongolia, China: Termination of the central

Asian orogenic belt: Tectonics, v. 22, p. 1069, doi:10.1029/2002TC001484.

Xu, Y. G., 2002, Evidence for crustal components in the mantle and constraints on crustal

recycling mechanisms: pyroxenite xenoliths from Hannuoba, North China: Chemical

Geology, v. 182, p. 301-322, doi: 10.1016/S0009-2541(01)00300-X.

Yan, G.H., Mu, B.L., Zeng, Y.S., Cai, J.H., Ren, K.X., and Li, F.T., 2007, Igneous

Carbonatites in North China Craton: The Temporal and Spatial Distribution, Sr and

Nd Isotopic Charateristics and Their Geological Significance (in Chinese with English

abstract): Geological Journal of China Universities, v. 13, p. 463–473.

Zhao, D.P., Tian, Y., Lei, J.S., Liu, L., and Zheng, S.H., 2009, Seismic image and origin of

the Changbai intraplate volcano in East Asia: Role of big mantle wedge above the

stagnant Pacific slab: Physics of the Earth and Planetary Interiors, v. 173, p. 197–206,

doi:10.1016/j.pepi.2008.11.009.

Zhi, X.C., Song, Y., Frey, F.A., Feng, J.L., and Zhai, M.Z., 1990, Geochemistry of

Hannuoba basalts, eastern China: Constraints on the origin of continental alkalic and

tholeiitic basalt: Chemical Geology, v. 88, p. 1–33,

doi:10.1016/0009-2541(90)90101-C.

Zhu, B.Q., 1998, Theory and applications of isotope systematics in geosciences: evolution

of continental crust and mantle in China (in Chinese): Beijing, Science Press.

Zhu, R.X., Chen, L., Wu, F.Y., and Liu, J.L., 2011, Timing, scale and mechanism of the

destruction of the North China Craton: Science China. Earth Sciences, v. 54,

p. 789–797, doi:10.1007/s11430-011-4203-4.

FIGURE CAPTIONS

Figure 1. (A) Tectonic framework of the study area (modified from Windley et al., 2010).

CAOB = Central Asian Orogenic Belt, QDSOB = Qinling-Dabie-Sulu Orogenic Belt, (B)

Field appearance of the carbonatite intrusion. (C) Residual Ol xenocryst partly resorbed by

carbonatite melt. (D) Monomineralic aggregates consist of interlocking calcite grains. CM

= carbonate matrix and SC = sparry calcite.

Figure 2. Primitive mantle (PM) normalized trace element patterns for Hannuoba

carbonatite intrusion compared to average carbonatite (ACarb) and average limestone

(AL) (data sources in the supplementary information). The Mesozoic Zhuolu (ZL) and

Huairen (HR) carbonatites are from Yan et al. (2007), and primitive mantle values from

McDonough and Sun (1995).

Figure 3. (A) Carbonates in the carbonatite intrusion lie on a trend between pure calcite and

peridotite, in contrast to limestones, which vary in CaO at constantly low Ni. (B) Plot of

$(^{87}Sr/^{86}Sr)_I$ - $(^{143}Nd/^{144}Nd)_I$. Age of the carbonatite intrusion was assumed to be the same as

the Hannuoba basalt (22Ma). $^{143}Nd/^{144}Nd$ ratios of aragonite veinlets (gray bar) are

represented by the intrusion. Solid curves are mixing lines between limestone and

Hannuoba peridotite (Per), ticks on curves show 10% increments. HSr-Carb = carbonatite

with Sr >60 ppm, LSr-Carb = carbonatite with Sr <60 ppm. G-Pyr = Hannuoba garnet

pyroxenite, Basalt = Hannuoba alkali basalts. Other symbols as in Figure 2. See

supplementary information for detailed explanation, data sources and modeling

parameters.

Figure 4. Schematic illustration of recycling of sedimentary limestone caused by

subduction of the PAOS. Symbol key as in Figure 2.

[1]GSA Data Repository item 2016xxx, xxxxxxxx, is available online at

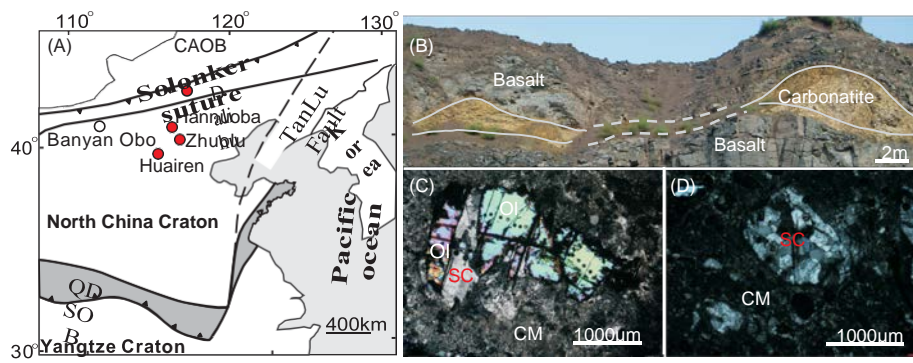http://www.geosociety.org/pubs/ft2016.htm or on request from editing@geosociety.org.
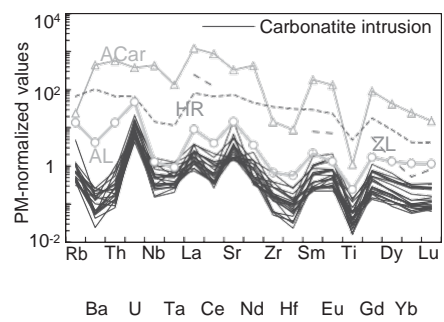
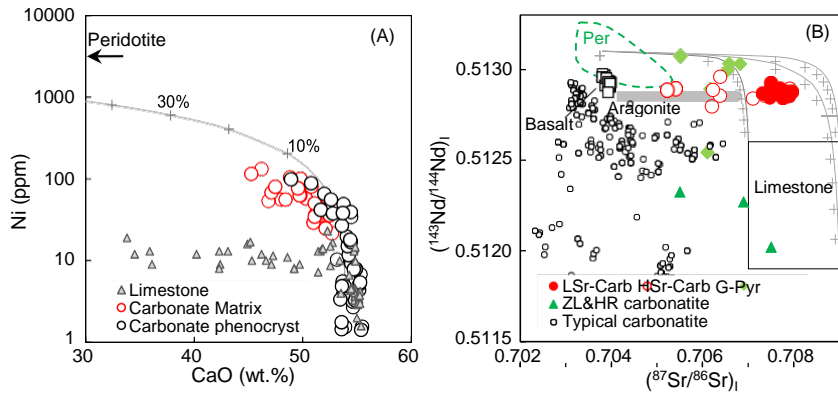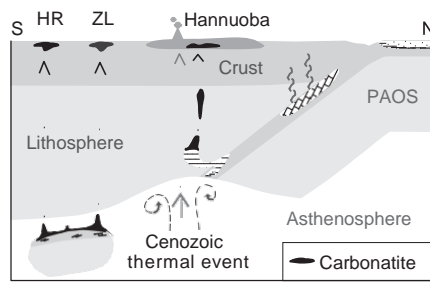Figure 1

Figure 2

Figure 3

Figure 4

Paleo-Asian Oceanic slab under the North China Craton revealed by carbonatites derived from subducted limestones

Chunfei Chen[1], Yongsheng Liu[1*], Stephen F. Foley[2], Mihai N. Ducea[3,4], Detao He[1], Zhaochu Hu[1], Wei Chen[1], Keqing Zong[1]

[1] State Key Laboratory of Geological Processes and Mineral Resources, School of Earth Sciences, China University of Geosciences, Wuhan 430074, China

[2] ARC Centre of Excellence for Core to Crust Fluid Systems, Dept. of Earth and Planetary Sciences, Macquarie University, North Ryde, New South Wales 2109, Australia.

[3] Department of Geosciences, University of Arizona, Tucson, AZ 85721, USA

[4] Faculty of Geology and Geophysics, University of Bucharest, Bucharest, Romania

Analytical methods

Whole rock samples were crushed in a corundum jaw crusher, and the resulting chips were handpicked to exclude the olivine, pyroxene and spinel xenocrysts. About 100g of the sample was then powdered in an agate ring mill to less than 200 mesh.

The sample powders were digested by $HF + HNO_3$ in Teflon bombs and analyzed using an Agilent 7500a ICP-MS at the State Key Laboratory of Geological Processes and Mineral Resources, China University of Geosciences, Wuhan (SKL GPMR-CUG). The detailed sample digestion procedure for ICP-MS analysis is given in Liu et al. (2008a). Analyses of rock standards (BCR-2, BHVO-2 and AGV-2) indicate accuracies are better than 5% for major elements and 10% for trace elements.

The selected samples were leached using 1N acetic acid to dissolve carbonate for Sr and Nd isotopic analyses. The leachate is believed to be the bulk carbonate component in the carbonatite. The chemical separation for Sr and Nd isotopic analyses is the same as the description by Gao et al. (2004). Sr-Nd isotopic ratios were determined using a Triton Ti TIMS at the SKL GPMR-CUG. The measured $^{143}Nd/^{144}Nd$ and $^{87}Sr/^{86}Sr$ ratios were normalized to $^{146}Nd/^{144}Nd = 0.7219$ and $^{88}Sr/^{86}Sr = 8.375209$, respectively. BCR-2 and GBW04411 were used as the monitor Standard materials in this work. Our analytical results ($^{143}Nd/^{144}Nd = 0.512629 \pm 0.000006$ (2σ) for BCR-2 and $^{87}Sr/^{86}Sr = 0.760033 \pm 0.000016$ (2σ) for GBW04411) fit the recommend values ($^{143}Nd/^{144}Nd = 0.512636 \pm 0.000002$ (2SD) for BCR-2; $^{87}Sr/^{86}Sr = 0.76 \pm 0.000006$ (2SD) for GBW04411) within analytical uncertainty.

Major and trace elements of silicate minerals, carbonate matrix and phenocrysts were

analyzed by LA-ICP-MS with a spot size of 44 µm at the SKL GPMR-CUG. Element contents were calibrated against multiple reference materials without applying internal standardization. Details of operating conditions for LA-ICP-MS and data reduction strategy are same as Liu et al. (2008b) for silicate minerals and Chen et al. (2011) for carbonate. Off-line selection and integration of the background and the analyzed signals, along with time-drift correction and quantitative calibration, were performed by ICPMSDataCal (Liu et al., 2008b).

The polished sections were prepared for identifying moissanite and highly disordered graphite using a Thermo Scientific DRX dispersive Raman micro-spectrometer. In order to avoid possible contamination, Al_2O_3 abrasive papers only were used to prepare the polished sections. The detailed sample preparation procedure is given in Liu et al. (2015).

Data sources for carbonatite and limestone

Carbonatites are compiled from a worldwide database (Bühn, 2008; Bell et al., 1982; Bell and Simonetti, 2010; Halama et al., 2008; Hoernle et al., 2002; Hou et al., 2015; Huang et al., 1995; Mitchell, 2005; Mourao et al., 2010).

Major elements in limestone were collected from worldwide (Armstrong-Altrin et al., 2003; Bellanca et al., 1997; Jin et al., 2009; Klein and Beukes, 1989; Tanaka et al., 2003; Tsikos et al., 2001). Trace elements in limestone collected from worldwide (Bellanca et al., 1997; Jin et al., 2009; Tanaka et al., 2003; Tsikos et al., 2001) are shown for comparison.

Detailed explanation, data sources and modelling parameters for Fig. 3

The CaO versus Ni plot in Fig.3 (A) shows that the carbonates in the carbonatite intrusion trend to high Ni contents, in contrast to limestones. The solid curve is a simple mixing line between limestone and the Hannuoba peridotite (Rudnick et al., 2004): ticks on curves show 10% increments. Average of peridotites from Hannuoba (Rudnick et al., 2004) is shown for comparison.

(B) Sr-Nd isotopic compositions of the Hannuoba intrusion (this paper). Aragonite veinlets (this paper), limestone (Keto and Jacobsen, 1988; Veizer et al., 1999), typical carbonatites (Bühn, 2008; Bell et al., 1982; Bell and Simonetti, 2010; Halama et al., 2008; Hoernle et al., 2002; Hou et al., 2015; Huang et al., 1995; Mitchell, 2005; Mourao et al., 2010), the Mesozoic carbonatites from Zhuolu (ZL) and Huairen (HR) (Yan et al., 2007), peridotite and garnet pyroxenite xenoliths (Rudnick et al., 2004; Xu, 2002), and alkali basalt (Song et al., 1990) from Hannuoba are shown for comparison. Average Sr and Nd contents (Sr=380 ppm; Nd=0.66 ppm) in Silurian, Devonian and Carboniferous limestones from the Inner Mongolia derived from the Paleo-Asian Ocean (Liu, et al. unpublished data) were used in model calculations. Detailed parameters are listed in the table below.

The trend to high Ni contents shown by the carbonates could reflect mixing in of a lower proportion of peridotite (~10%) (Fig. 3A) than that of the trend to high $^{143}Nd/^{144}Nd$ (~30%) (Fig. 3B). This could be attributed to the transfer of Ni from carbonatite melt to newly growth silicate minerals (i.e. clinopyroxene) during carbonatite-peridotite interaction.

Compositional parameters	Sr	Nd
Limestone (ppm)	380	0.66
Limestone isotope ratios	0.707-0.709	0.5119-0.5123
Average of Hannuoba peridotites (ppm)	14.6	1.09
Average of Hannuoba peridotites isotopic ratios	0.7038	0.51310

Figure DR1
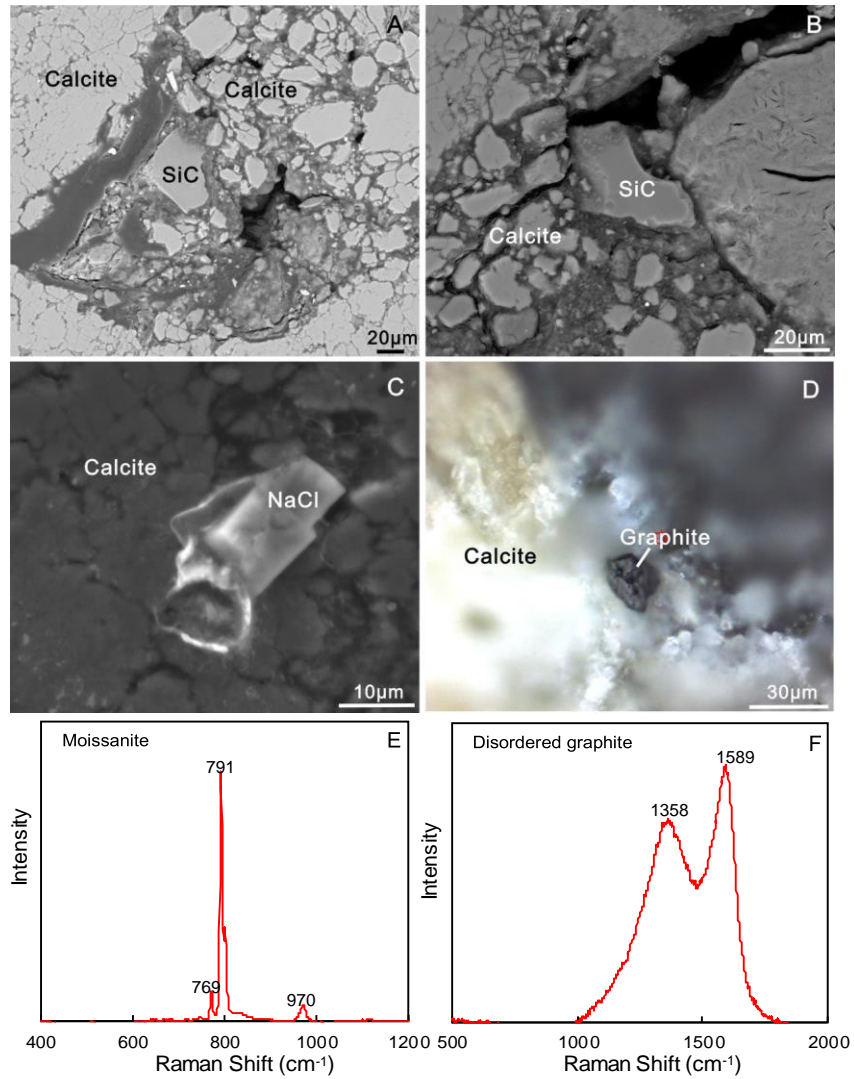
Moissanite (A and B), Na chloride (C) and graphite (D) coexisting with carbonate in the carbonatite intrusion. Raman shift of moissanite (E) and highly disordered graphite (F) in the carbonatite intrusion.

Figure DR2
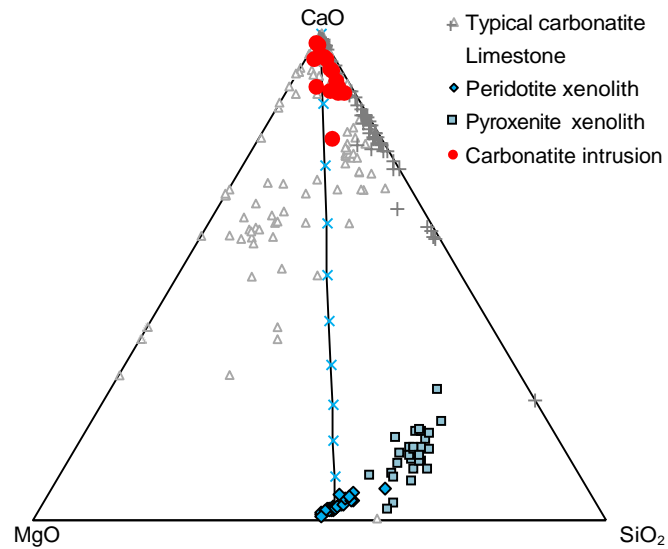
CaO-MgO-SiO$_2$ diagram of the Hannuoba carbonatite intrusion (red circles). The solid line with crosses is a mixing line showing 10% increments between pure limestone and peridotite. Peridotite xenoliths (Rudnick et al., 2004) and pyroxenite veins (Liu et al., 2005; Xu, 2002) in peridotite xenoliths from Hannuoba, limestone (Armstrong-Altrin et al., 2003; Bellanca et al., 1997; Jin et al., 2009; Klein and Beukes, 1989; Tanaka et al., 2003; Tsikos et al., 2001) and typical carbonatites (Bühn, 2008; Bell et al., 1982; Bell and Simonetti, 2010; Halama et al., 2008; Hoernle et al., 2002; Hou et al., 2015; Huang et al., 1995; Mitchell, 2005; Mourao et al., 2010)   are shown for comparison.

Figure DR3
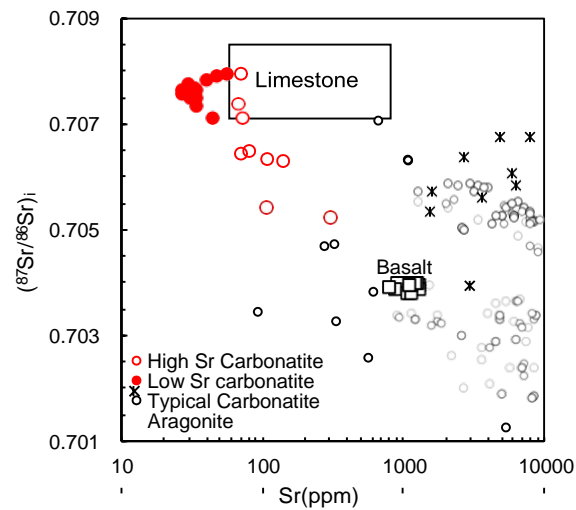
Variations of $({}^{87}Sr/{}^{86}Sr)_I$ with Sr contents for carbonates and aragonite veins in the Hannuoba carbonatite intrusion. The carbonatite intrusion can be classified into two types: low Sr carbonatite (Sr 30~50 ppm) and high Sr carbonatite (Sr >60 ppm). The isotopic compositions are calculated back to 22 Ma (age of the Hannuoba basalt). The typical carbonatites (data sources as in Figure DR2) and alkali basalts from Hannuoba are shown for comparison. Sr isotopic data for limestone are from Veizer et al. (1999).

Figure DR4
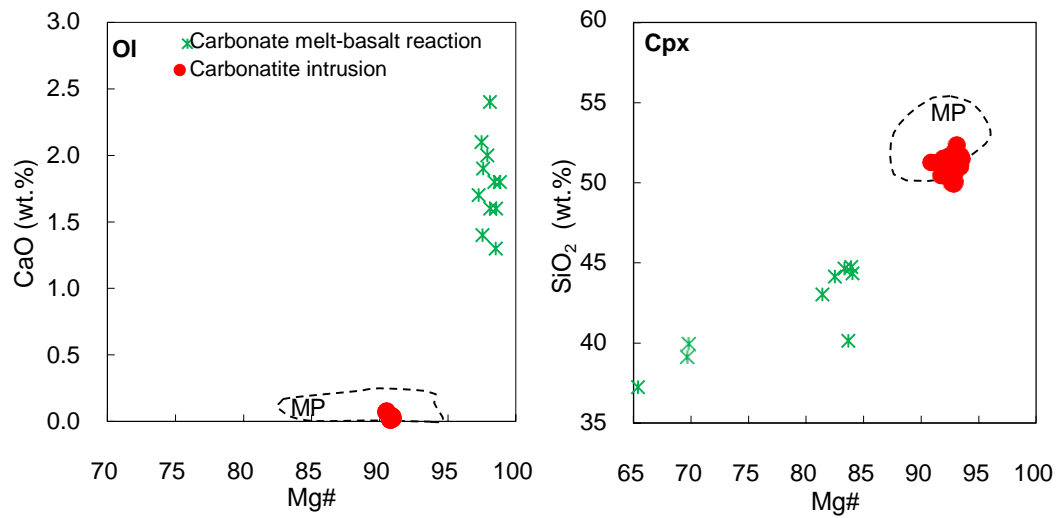
Plots of Mg# versus CaO and SiO₂ for Ol and Cpx xenocrysts from the Hannuoba carbonatite intrusion, eliminating the possibility that the carbonatite composition could be due to interaction between carbonate and basaltic melt. Data for Ol and Cpx formed by carbonate melt-basalt interaction are from Jolis et al. (2013). MP = Range of mantle peridotites from the North China Craton (e.g., Rudnick et al., 2004; Xu et al., 2013).

Figure DR5
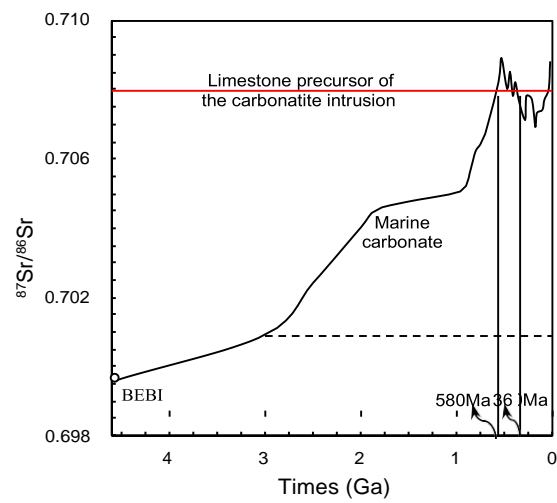
(^{87}Sr/ ^{86}Sr)$_I$ comparison between the limestone precursor of the Hannuoba carbonatite and the evolution line of marine carbonates (Veizer, 1985; Veizer et al., 1999). The intersection points infer that the limestone precursor of the carbonatite intrusion was certainly not older than 580 Ma, and most probably between 360 and 580 Ma. BEBI = Bulk-Earth best initial.

References not cited in main paper

The temperatures of silicate macrocrysts were estimated using thermometer of Cpx + Opx pairs (Wells, 1977).

(Burke et al., 2003)

Table DR 1

Compositions of silicate mineral xenocrysts in the Hannuoba carbonatite intrusion
Units are wt.% for major elements and ppm for Ni.

Num.	JSB011		JSB029			JSB012		JSB024			JSB044		JSB054	
	Cpx	Opx	Cpx	Ol	Opx	Cpx	Opx	Cpx	Opx	Ol	Cpx	Opx	Cpx	Opx
SiO_2	51.2	54.8	50.8	39.0	54.5	50.1	55.4	51.3	55.4	39.5	50.6	54.3	51.1	55.7
TiO_2	0.30	0.08	0.11	0.00	0.04	0.33	0.07	0.29	0.08	0.00	0.32	0.08	0.34	0.08
Al_2O_3	5.18	3.79	4.40	0.03	4.04	5.88	3.46	5.00	3.35	0.01	5.75	4.15	4.69	3.47
TFeO	2.36	5.27	2.68	9.15	5.97	2.21	6.11	2.07	5.70	9.12	2.25	5.59	2.70	5.76
MnO	0.08	0.13	0.09	0.14	0.14	0.07	0.14	0.08	0.14	0.13	0.08	0.13	0.08	0.14
MgO	16.7	34.6	17.7	51.2	33.5	15.9	33.8	16.3	34.1	50.7	16.2	34.3	17.2	33.5
CaO	21.6	0.65	22.5	0.08	0.98	22.9	0.46	22.3	0.51	0.03	21.9	0.61	21.3	0.62
Na_2O	1.39	0.08	0.62		0.05	1.44	0.05	1.34	0.06		1.54	0.07	1.32	0.1
K_2O	0.00	0.00	0.01	0.00	0.00	0.00	0.00	0.00	0.00	0.00	0.00	0.00	0.01	0.00
P_2O_5	0.01	0.01	0.01	0.02	0.01	0.01	0.01	0.01	0.01	0.01	0.01	0.01	0.02	0.01
Mg#	92.6	92.1	92.2	90.9	90.9	92.8	90.8	93.3	91.4	90.8	92.8	91.6	91.9	91.2
Ni	348	734	376	2809	809	287	691	308	713	3062	327	715	378	755

Table DR 2

Major and trace element, Sr-Nd isotopic and C-O isotopic compositions of carbonate components in carbonatite intrusion. Units are wt.% for major elements, ppm for trace elements and ‰ for C-O isotopes.

Num.	Carbonatite intrusion (JSB-)										
	12011	12022	12023	12029	12032	12033	12044	12046	12049	12051	12053
SiO_2	5.04	3.12	3.33	5.31	2.05	4.48	4.91	4.44	0.31	1.88	6.32
TiO_2	0.008	0.004	0.029	0.012	0.006	0.003	0.012	0.013	0.006	0.003	0.012
Al_2O_3	0.73	0.51	0.60	0.42	0.40	0.59	1.24	1.45	0.42	0.66	1.19
FeO	1.41	1.03	1.57	1.63	1.32	1.55	1.11	1.30	1.17	1.04	1.28
MgO	1.39	0.90	1.04	1.58	0.88	1.08	1.35	2.18	0.80	0.85	1.59
CaO	50.1	52.3	51.4	49.7	52.7	50.8	50.2	49.2	53.9	52.9	49.0
Na_2O	0.007	0.013	0.006	0.016	0.01	0.008	0.008	0.014	0.005	0.009	0.013
K_2O	0.019	0.014	0.02	0.023	0.014	0.017	0.014	0.016	0.012	0.026	0.016
Sc	1.02	0.40	0.97	2.25	0.89	0.80	0.69	0.65	0.36	0.29	0.80
V	2.68	1.94	2.73	2.36	1.70	3.25	2.23	3.36	1.11	1.38	2.60
Cr	61.5	35.4	56.4	104	91.5	285	16.5	57.8	8.47	2.39	125
Co	4.02	1.22	3.50	6.11	2.63	3.60	1.10	7.35	3.46	1.48	10.0
Ni	113	58.3	118	169	98.6	113	74.4	181	132	96.7	145
Rb	0.69	0.25	0.67	0.41	0.24	0.58	0.29	0.38	0.27	0.65	0.41
Sr	32.4	27.5	30.6	34.2	29.8	34.3	31.7	55.7	34.1	47.0	79.1
Y	1.72	1.20	1.29	1.68	1.16	0.87	2.30	0.53	0.56	0.55	0.50
Zr	2.04	0.70	4.04	1.71	0.65	0.65	2.91	2.88	1.60	1.68	1.71
Nb	0.21	0.15	0.77	0.39	0.18	0.10	0.34	0.55	0.20	0.36	0.41
Ba	0.44	0.39	0.35	0.82	0.16	0.28	0.35	1.26	0.35	1.07	1.48
La	1.44	1.66	1.48	1.56	1.53	1.10	2.36	0.56	0.57	0.88	0.48
Ce	1.34	1.73	2.24	2.16	1.91	0.83	3.54	0.67	0.58	0.69	0.63
Pr	0.37	0.27	0.31	0.39	0.27	0.15	0.62	0.11	0.11	0.12	0.095
Nd	1.73	1.16	1.43	1.79	1.12	0.69	2.85	0.49	0.46	0.48	0.43
Sm	0.43	0.22	0.35	0.42	0.23	0.14	0.73	0.099	0.10	0.10	0.089
Eu	0.25	0.12	0.13	0.20	0.12	0.089	0.32	0.049	0.056	0.042	0.034
Gd	0.41	0.23	0.28	0.40	0.26	0.15	0.60	0.11	0.10	0.098	0.079
Tb	0.07	0.03	0.04	0.06	0.03	0.02	0.08	0.01	0.01	0.01	0.01
Dy	0.36	0.14	0.22	0.30	0.14	0.11	0.43	0.081	0.080	0.059	0.078
Ho	0.07	0.03	0.04	0.05	0.03	0.02	0.08	0.01	0.02	0.01	0.02
Er	0.17	0.063	0.094	0.12	0.071	0.050	0.19	0.036	0.040	0.029	0.034
Tm	0.028	0.008	0.011	0.019	0.009	0.006	0.024	0.005	0.005	0.004	0.004
Yb	0.15	0.045	0.081	0.12	0.056	0.044	0.13	0.027	0.036	0.025	0.035
Lu	0.023	0.008	0.011	0.018	0.009	0.005	0.019	0.005	0.004	0.005	0.005
Hf	0.021	0.009	0.078	0.029	0.014	0.007	0.036	0.041	0.016	0.019	0.027
Ta	0.013	0.010	0.044	0.021	0.013	0.010	0.020	0.026	0.012	0.009	0.020
Pb	0.10	0.051	0.12	0.39	0.11	0.076	0.094	0.13	0.080	0.10	0.10
Th	0.02	0.01	0.06	0.03	0.01	0.01	0.02	0.02	0.01	0.03	0.02
U	0.15	0.087	0.11	0.12	0.11	0.15	0.17	0.34	0.15	0.29	0.24
Ce/Ce*	0.45	0.63	0.80	0.68	0.72	0.50	0.71	0.66	0.56	0.51	0.71
Eu/Eu*	1.78	1.62	1.17	1.50	1.42	1.80	1.44	1.40	1.62	1.27	1.21
$^{87}Rb/^{86}Sr$	0.0598	0.0256	0.0621	0.0338	0.0223	0.0476	0.0258	0.0192	0.0222	0.0387	0.0145
$^{87}Sr/^{86}Sr$	0.707496	0.707576	0.707780	0.707343	0.707710	0.707640	0.707509	0.707963	0.707509	0.707902	0.706383
2σ	4	5	5	6	5	7	5	5	17	18	5
$^{147}Sm/^{144}Nd$	0.1564	0.1218	0.1539	0.1479	0.1308	0.1321	0.1600	0.1274	0.1427	0.1306	0.1293
$^{143}Nd/^{144}Nd$	0.512869	0.512884	0.512866	0.512887	0.51291	0.512885	0.512909	0.512894	0.512941	0.512872	0.512874
2σ	5	4	8	4	4	9	4	7	16	12	13
$\delta^{13}C_{VPDB}$	-12.0	-12.4	-12.6	-13.1	-11.9	-12.1	-11.9	-11.4	-12.8	-11.3	-12.2
$\delta^{18}O_{SMOW}$	22.7	22.8	22.6	22.6	22.8	22.8	22.7	22.7	22.5	22.6	22.3

Table DR 2 continued

	Carbonatite intrusion (JSB-)									
Num.	12055	12057	12058	12061	12063	12093	14005	14035	14045	14009
SiO_2	7.55	2.20	0.92	5.91	2.59	3.76	7.36	3.68	16.00	2.70
TiO_2	0.026	0.011	0.023	0.008	0.009	0.003	0.016	0.008	0.008	0.005
Al_2O_3	1.76	0.55	1.16	0.80	0.86	0.44	1.86	0.42	0.51	1.37
FeO	1.27	1.13	1.64	1.13	0.91	1.17	1.28	1.45	0.52	0.73
MgO	3.00	1.18	2.03	1.10	1.43	1.24	4.81	1.56	2.03	3.35
CaO	46.4	52.3	51.2	50.2	51.8	51.4	44.2	50.8	44.1	49.4
Na_2O	0.012	0.005	0.012	0.006	0.009	0.006	0.03	0.009	0.011	0.014
K_2O	0.015	0.013	0.02	0.013	0.024	0.014	0.012	0.012	0.039	0.013
Sc	0.70	0.37	0.95	0.42	0.40	0.52	1.57	0.80	0.36	0.40
V	3.10	1.63	3.51	1.25	1.58	1.47	7.08	3.41	1.70	1.70
Cr	56.2	11.0	84.2	21.6	1.48	9.75	181	112	13.6	21.7
Co	5.17	4.33	6.01	2.72	1.79	1.79	8.75	3.00	1.74	1.51
Ni	127	129	198	119	93.3	94.1	208	152	156	83.9
Rb	0.41	0.30	0.45	0.27	0.74	0.43	0.19	0.32	2.84	0.22
Sr	109	106	40.1	33.8	306	68.7	64.7	72.9	138	63.3
Y	1.82	0.69	0.94	0.62	0.62	3.26	1.83	0.86	0.45	0.72
Zr	6.76	2.02	2.92	1.77	3.98	1.45	1.26	1.30	1.67	0.54
Nb	1.06	0.34	0.63	0.31	0.78	0.10	0.22	0.17	0.31	0.21
Ba	1.45	0.44	0.86	0.39	1.71	1.71	0.92	1.01	1.07	0.67
La	2.46	0.93	1.03	0.73	0.89	2.31	1.39	0.72	0.81	1.15
Ce	2.82	1.09	1.58	0.96	1.07	0.55	0.45	0.56	0.57	0.95
Pr	0.41	0.15	0.23	0.14	0.15	0.31	0.23	0.10	0.11	0.15
Nd	1.73	0.67	0.97	0.67	0.65	1.38	1.06	0.46	0.40	0.58
Sm	0.38	0.15	0.24	0.16	0.12	0.25	0.28	0.11	0.087	0.11
Eu	0.26	0.074	0.088	0.067	0.076	0.12	0.13	0.045	0.080	0.044
Gd	0.38	0.14	0.22	0.15	0.14	0.37	0.30	0.12	0.072	0.11
Tb	0.048	0.022	0.031	0.021	0.019	0.043	0.042	0.017	0.011	0.014
Dy	0.27	0.098	0.16	0.12	0.12	0.26	0.26	0.099	0.066	0.081
Ho	0.050	0.019	0.028	0.018	0.019	0.056	0.045	0.021	0.013	0.016
Er	0.13	0.047	0.076	0.050	0.040	0.16	0.13	0.051	0.040	0.040
Tm	0.019	0.007	0.010	0.005	0.007	0.023	0.017	0.007	0.007	0.0057
Yb	0.12	0.045	0.055	0.040	0.038	0.14	0.11	0.044	0.041	0.030
Lu	0.016	0.005	0.010	0.006	0.006	0.023	0.018	0.007	0.008	0.006
Hf	0.073	0.033	0.053	0.029	0.037	0.009	0.027	0.017	0.024	0.010
Ta	0.046	0.018	0.038	0.014	0.019	0.008	0.013	0.010	0.024	0.028
Pb	0.12	0.082	0.16	0.066	0.22	0.11	0.063	0.088	0.22	0.082
Th	0.043	0.020	0.078	0.013	0.059	0.015	0.013	0.008	0.027	0.007
U	0.29	0.11	0.13	0.16	0.44	0.19	0.19	0.20	0.32	0.18
Ce/Ce*	0.68	0.71	0.79	0.71	0.71	0.16	0.19	0.51	0.46	0.56
Eu/Eu*	2.07	1.51	1.15	1.29	1.82	1.23	1.33	1.15	2.98	1.19
$^{87}Rb/^{86}Sr$	0.0105	0.0079	0.0313	0.0224	0.0069	0.0177	0.0082	0.0125	0.0578	0.0098
$^{87}Sr/^{86}Sr$	0.706225	0.705401	0.707822	0.707681	0.705222	0.707374	0.707908	0.707108	0.706217	0.706388
2σ	6	5	5	6	5	6	5	5	14	10
$^{147}Sm/^{144}Nd$	0.1394	0.1413	0.1554	0.1459	0.1141	0.1145	0.1644	0.1562	0.1351	0.1214
$^{143}Nd/^{144}Nd$	0.512906	0.512912	0.5129	0.512903	0.512902	0.512871	0.512918	0.512862	0.512817	0.512976
2σ	6	4	5	4	6	5	7	14	6	23
$\delta^{13}C_{VPDB}$	-12.7	-14.4	-13.5	-13.3	-13.6	-11.3	-11.9	-11.8	-11.4	-11.2
$\delta^{18}O_{SMOW}$	22.2	22.6	22.6	22.6	22.6	23.0	22.6	22.5	22.6	23.0

Based on the normalization strategy of bulk components as 100%, SiO_2^* is calculated by 100%-
the sum of all other major element concentrations expressed as carbonates.

Table DR 3

Compositions of calcite phenocryst (CP) and calcite matrix (CM) in the Hannuoba carbonatite intrusion. Units are wt.% for major elements and ppm for Ni.

Sample Name		CaO	MgO	FeO	SiO_2	Al_2O_3	Ni
JSB011-Cc1-01	CP	55.3	0.23	0.08	0.20	0.00	6.8
JSB011-Cc1-02	CP	55.5	0.20	0.05	0.18	0.00	1.6
JSB011-Cc1-03	CP	55.4	0.22	0.04	0.26	0.00	1.4
JSB012-Cc1-01	CP	53.8	0.58	0.18	0.91	0.01	49.2
JSB012-Cc1-02	CP	54.5	0.48	0.10	0.61	0.00	34.4
JSB012-Cc1-03	CP	54.4	0.61	0.08	0.50	0.00	39.4
JSB012-Cc2-01	CP	54.7	0.60	0.03	0.44	0.00	2.7
JSB012-Cc2-02	CP	54.6	0.68	0.03	0.40	0.00	3.2
JSB012-Cc2-03	CP	54.8	0.59	0.03	0.34	0.00	3.3
JSB024-Cc1-01	CP	53.7	1.42	0.06	0.36	0.00	3.9
JSB024-Cc1-02	CP	53.5	1.62	0.06	0.41	0.00	3.4
JSB024-Cc1-03	CP	53.9	1.33	0.08	0.28	0.00	1.5
JSB024-Cc2-01	CP	54.5	0.63	0.07	0.49	0.01	9.3
JSB024-Cc2-02	CP	54.5	0.45	0.13	0.58	0.02	13.2
JSB024-Cc2-03	CP	54.9	0.36	0.07	0.42	0.01	8.0
JSB029-Cc1-01	CP	53.6	1.63	0.08	0.28	0.00	1.5
JSB029-Cc1-02	CP	53.6	1.59	0.09	0.31	0.00	1.8
JSB029-Cc1-03	CP	53.2	1.65	0.12	0.50	0.02	10.3
JSB029-Cc2-01	CP	54.2	0.58	0.12	0.64	0.03	11.7
JSB029-Cc2-02	CP	48.9	1.04	0.98	3.30	0.21	98.9
JSB044-Cc1-04	CP	53.7	1.61	0.02	0.30	0.00	5.6
JSB044-Cc1-05	CP	53.9	1.54	0.02	0.21	0.00	4.9
JSB044-Cc1-06	CP	53.6	1.74	0.02	0.23	0.00	4.9
JSB044-Cc2-03	CP	54.8	0.26	0.09	0.53	0.04	8.0
JSB044-Cc2-04	CP	54.9	0.39	0.08	0.40	0.03	7.9
JSB044-Cc2-05	CP	51.6	0.46	0.50	1.99	0.40	41.8
JSB044-Cc2-06	CP	54.2	0.26	0.20	0.81	0.13	15.0
JSB054-Cc1-01	CP	54.7	0.30	0.06	0.48	0.08	7.9
JSB054-Cc1-02	CP	54.9	0.47	0.03	0.33	0.01	4.4
JSB054-Cc3-05	CP	54.0	0.43	0.18	0.84	0.05	19.7
JSB054-Cc3-06	CP	54.4	0.53	0.12	0.55	0.03	17.0
JSB054-Cc3-07	CP	52.8	0.44	0.42	1.39	0.17	37.9
JSB054-Cc3-08	CP	53.6	0.31	0.24	1.07	0.16	26.9
JSB054-Cc3-09	CP	55.2	0.31	0.03	0.30	0.00	4.4
JSB054-Cc3-10	CP	54.4	0.39	0.16	0.70	0.04	18.0
JSB057-Cc3-02	CP	55.2	0.19	0.07	0.32	0.00	5.1
JSB057-Cc3-03	CP	55.3	0.20	0.06	0.29	0.00	5.4
JSB057-Cc1-01	CP	52.0	0.53	0.53	1.79	0.16	65.8
JSB057-Cc1-02	CP	52.6	0.40	0.43	1.59	0.19	55.7
JSB057-Cc1-03	CP	53.7	0.32	0.31	1.05	0.07	38.1
JSB057-Cc1-04	CP	50.8	0.45	0.72	2.54	0.34	88.6

Table DR 3 continued

Sample Name		CaO	MgO	FeO	SiO$_2$	Al$_2$O$_3$	Ni
JSB011-Cc2-01	CM	51.2	0.48	0.94	2.31	0.11	36.8
JSB011-Cc2-02	CM	51.1	0.48	0.98	2.27	0.14	36.1
JSB011-Cc2-03	CM	52.7	0.41	0.58	1.54	0.08	21.7
JSB011-Cc2-04	CM	52.1	0.48	0.74	1.78	0.08	24.7
JSB024-Cc3-01	CM	51.6	0.54	0.79	2.06	0.05	36.0
JSB024-Cc3-02	CM	49.8	0.69	1.15	2.97	0.08	62.9
JSB024-Cc3-03	CM	50.3	0.69	1.06	2.74	0.06	57.5
JSB024-Cc3-04	CM	48.8	0.72	1.27	3.53	0.14	104
JSB024-Cc3-05	CM	49.8	0.62	1.07	3.10	0.11	101
JSB029-Cc1-01	CM	48.0	1.03	1.57	3.74	0.08	55.9
JSB029-Cc1-02	CM	46.8	1.20	1.85	4.30	0.06	54.2
JSB044-Cc1-01	CM	51.0	0.47	0.88	2.37	0.23	29.1
JSB044-Cc1-02	CM	47.1	0.90	1.49	4.12	0.49	68.3
JSB044-Cc1-03	CM	46.2	0.91	1.81	4.63	0.43	133
JSB044-Cc1-07	CM	51.5	0.53	0.82	2.00	0.18	44.7
JSB044-Cc1-08	CM	51.6	0.51	0.79	2.03	0.16	38.4
JSB044-Cc2-01	CM	51.1	0.60	0.85	2.24	0.22	34.7
JSB044-Cc2-02	CM	48.4	0.66	1.56	3.64	0.23	56.2
JSB054-Cc3-01	CM	47.5	0.74	1.07	4.00	0.82	80.5
JSB054-Cc3-02	CM	49.8	0.63	0.79	2.91	0.50	62.9
JSB054-Cc3-03	CM	49.7	0.60	0.77	2.99	0.50	63.2
JSB054-Cc3-04	CM	51.1	0.52	0.74	2.33	0.26	50.0
JSB057-Cc3-01	CM	52.5	0.47	0.60	1.65	0.02	35.8
JSB057-Cc3-04	CM	50.8	0.62	0.93	2.48	0.04	80.5
JSB054-Cc1-03	CM	49.6	1.11	0.69	2.89	0.31	76.5
JSB054-Cc1-04	CM	45.2	1.80	0.87	4.97	0.70	116

Table DR 4

Sr content and Sr isotopic compositions of aragonite veinlets crosscutting one sample of the carbonatite intrusion.

Sample	Sr (ppm)	$^{87}Sr/^{86}Sr$	2σ
JSB15062-1	6022	0.70605	0.000015
JSB15062-2	1610	0.70571	0.000039
JSB15062-3	2700	0.70635	0.000034
JSB15062-4	4909	0.70673	0.000016
JSB15062-5	7848	0.70672	0.000013
JSB15062-6	3654	0.70560	0.000019
JSB15062-7	1545	0.70532	0.000047
JSB15062-8	6442	0.70583	0.000027
JSB15062-9	5005	0.70683	0.000017
JSB15062-10	5005	0.70684	0.000021
JSB15062-11	4941	0.70584	0.000030
JSB15062-13	3246	0.70411	0.000039

References

Armstrong-Altrin, J. S., Verma, S. P., Madhavaraju, J., Lee, Y. I., and Ramasamy, S., 2003, Geochemistry of Upper Miocene Kudankulam Limestones, Southern India: International Geology Review, v. 45, p. 16-26, doi: 10.2747/0020-6814.45.1.16.

Bühn, B., 2008, The role of the volatile phase for REE and Y fractionation in low-silica carbonate magmas: implications from natural carbonatites, Namibia: Mineralogy and Petrology, v. 92, p. 453-470, doi: 10.1007/s00710-007-0214-4.

Bell, K., Blenkinsop, J., Cole, T. J. S., and Menagh, D. P., 1982, Evidence from Sr isotopes for long-lived heterogeneities in the upper mantle: Nature, v. 298, p. 251-253, doi: 10.1038/298251a0.

Bell, K., and Simonetti, A., 2010, Source of parental melts to carbonatites–critical isotopic constraints: Mineralogy and Petrology, v. 98, p. 77-89, doi: 10.1007/s00710-009-0059-0.

Bellanca, A., Masetti, D., and Neri, R., 1997, Rare earth elements in limestone/marlstone couplets from the Albian-Cenomanian Cismon section (Venetian region, northern Italy) : assessing REE sensitivity to environmental changes: Chemical Geology, v. 141, p. 141-152, doi: 10.1016/S0009-2541(97)00058-2.

Burke, K., Ashwal, L. D., and Webb, S. J., 2003, New way to map old sutures using deformed alkaline rocks and carbonatites: Geology, v. 31, p. 391-394.

Chen, L., Liu, Y.S., Hu, Z. C., Gao, S., Zong, K. Q., and Chen, H. H., 2011, Accurate determinations of fifty-four major and trace elements in carbonate by LA-ICP-MS using normalization strategy of bulk components as 100%: Chemical Geology, v. 284, p. 283-295, doi: 10.1016/j.chemgeo.2011.03.007.

Gao, S., et al., 2004, Recycling lower continental crust in the North China craton: Nature, v. 432, p. 892-897, doi: 10.1038/nature03162.

Halama, R., McDonough, W. F., Rudnick, R. L., and Bell, K., 2008, Tracking the lithium isotopic evolution of the mantle using carbonatites: Earth and Planetary Science Letters, v. 265, p. 726-742, doi: 10.1016/j.epsl.2007.11.007.

Hoernle, K., Tilton, G., Le Bas, M., Duggen, S., and Garbe-Schönberg, D., 2002, Geochemistry of oceanic carbonatites compared with continental carbonatites: mantle recycling of oceanic crustal carbonate: Contributions to Mineralogy and Petrology, v. 142, p. 520-542, doi: 10.1007/s004100100308.

Hou, Z. Q., Liu, Y., Tian, S. H., Yang, Z. M., and Xie, Y.L., 2015, Formation of carbonatite-related giant rare-earth-element deposits by the recycling of marine sediments: Sci Rep, v. 5, p. 10231, doi: 10.1038/srep10231.

Huang, Y. M., Hawkesworth, C. J., van Calsteren, P., and McDermott, F., 1995, Geochemical characteristics and origin of the Jacupiranga carbonatites, Brazil: Chemical Geology, v. 119, p. 79-99, doi: 10.1016/0009-2541(94)00093-N.

Jin, Z. J., Zhu, D. Y., Hu, W. X., Zhang, X. F., Zhang, J. T., and Song, Y.C., 2009, Mesogenetic dissolution of the middle Ordovician limestone in the Tahe oilfield of Tarim basin, NW China: Marine and Petroleum Geology, v. 26, p. 753-763, doi: 10.1016/j.marpetgeo.2008.08.005.

Jolis, E. M., Freda, C., Troll, V. R., Deegan, F. M., Blythe, L. S., McLeod, C. L., and Davidson, J. P., 2013, Experimental simulation of magma–carbonate interaction beneath Mt. Vesuvius, Italy:

Contributions to Mineralogy and Petrology, v. 166, p. 1335-1353, doi: 10.1007/s00410-013-0931-0.

Keto, L. S., and Jacobsen, S. B., 1988, Nd isotopic variations of Phanerozoic paleoceans: Earth and Planetary Science Letters, v. 90, p. 395-410, doi: 10.1016/0012-821X(88)90138-0.

Klein, C., and Beukes, N. J., 1989, Geochemistry and sedimentology of a facies transition from limestone to iron-formation deposition in the early Proterozoic Transvaal Supergroup, South Africa.: Economic Geology, v. 84, p. 1733-1774.

Liu, Y. S., Gao, S., Lee, C.-T. A., Hu, S. H., Liu, X. M., and Yuan, H. L., 2005, Melt–peridotite interactions: Links between garnet pyroxenite and high-Mg# signature of continental crust: Earth and Planetary Science Letters, v. 234, p. 39-57, doi: 10.1016/j.epsl.2005.02.034.

Liu, Y. S., He, D. T., Gao, C. G., Foley, S. F., Gao, S., Hu, Z. C., Zong, K. Q., and Chen, H. H., 2015, First direct evidence of sedimentary carbonate recycling in subduction-related xenoliths: Scientific Reports, v. 5, p. 11547, doi: 10.1038/srep11547.

Liu, Y. S., Zong, K. Q., Kelemen, P. B., and Gao, S., 2008a, Geochemistry and magmatic history of eclogites and ultramafic rocks from the Chinese continental scientific drill hole: Subduction and ultrahigh-pressure metamorphism of lower crustal cumulates: Chemical Geology, v. 247, p. 133-153, doi: 10.1016/j.chemgeo.2007.10.016.

Liu, Y. S., Hu, Z. C., Gao, S., Guenther, D., Xu, J., Gao, C. G., and Chen, H. H., 2008b, In situ analysis of major and trace elements of anhydrous minerals by LA-ICP-MS without applying an internal standard: Chemical Geology, v. 257, p. 34-43, doi: 10.1016/j.chemgeo.2008.08.004.

Mitchell, R. H., 2005, Carbonatites and carbonatites and carbonatites.: The Canadian Mineralogist, v. 43, p. 2049-2068, doi: 10.2113/gscanmin.43.6.2049.

Mourao, C., Mata, J., Doucelance, R., Madeira, J., da Silveira, A. B., Silva, L. C., and Moreira, M., 2010, Quaternary extrusive calciocarbonatite volcanism on Brava Island (Cape Verde): A nephelinite-carbonatite immiscibility product: Journal of African Earth Sciences, v. 56, p. 59-74, doi: 10.1016/j.jafrearsci.2009.06.003.

Rudnick, R. L., Gao, S., Ling, W. L., Liu, Y. S., and McDonough, W. F., 2004, Petrology and geochemistry of spinel peridotite xenoliths from Hannuoba and Qixia, North China craton: Lithos, v. 77, p. 609-637, doi: 10.1016/j.lithos.2004.03.033.

Song, Y., Frey, F. A., and Zhi, X., 1990, Isotopic characteristics of Hannuoba basalts, eastern China: Implications for their petrogenesis and the composition of subcontinental mantle: Chemical Geology, v. 88, p. 35-52, doi: 10.1016/0009-2541(90)90102-D.

Tanaka, K., Miura, N., Asahara, Y., and Kawabe, I., 2003, Rare earth element and strontium isotopic study of seamount-type limestones in Mesozoic accretionary complex of Southern Chichibu Terrane, central Japan: Implication for incorporation process of seawater REE into limestones: Geochemical Journal, v. 37, p. 163-180.

Tsikos, H., Moore, J. M., and Harris, C., 2001, Geochemistry of the Palæoproterozoic Mooidraai Formation: Fe-rich limestone as end member of iron formation deposition, Kalahari Manganese Field, Transvaal Supergroup, South Africa: Journal of African Earth Sciences, v. 32, p. 19-27, doi: 10.1016/S0899-5362(01)90016-8.

Veizer, J., 1985, Carbonates and Ancient Oceans: Isotopic and Chemical Record on Time Scales of 107–109 Years, The Carbon Cycle and Atmospheric CO2: Natural Variations Archean to Present, American Geophysical Union, p. 595-601.

Veizer, J., et al., 1999, $^{87}Sr/^{86}Sr$, $\delta^{13}C$ and $\delta^{18}O$ evolution of Phanerozoic seawater: Chemical Geology, v.

161, p. 59-88, doi: 10.1016/S0009-2541(99)00081-9.

Wells, P. R. A., 1977, Pyroxene thermometry in simple and complex systems: Contributions to Mineralogy and Petrology, v. 62, p. 129-139, doi: 10.1007/bf00372872.

Xu, R., Liu, Y. S., Tong, X. R., Hu, Z. C., Zong, K. Q., and Gao, S., 2013, In-situ trace elements and Li and Sr isotopes in peridotite xenoliths from Kuandian, North China Craton: Insights into Pacific slab subduction-related mantle modification: Chemical Geology, v. 354, p. 107-123, doi: 10.1016/j.chemgeo.2013.06.022.

Xu, Y. G., 2002, Evidence for crustal components in the mantle and constraints on crustal recycling mechanisms: pyroxenite xenoliths from Hannuoba, North China: Chemical Geology, v. 182, p. 301-322, doi: 10.1016/S0009-2541(01)00300-X.

Yan, G. H., Mu, B. L., Zeng, Y. S., Cai, J. H., Ren, K. X., and Li, F. T., 2007, Igneous Carbonatites in North China Craton: The Temporal and Spatial Distribution, Sr and Nd Isotopic Charateristics and Their Geological Significance (in Chinese with English abstract): Geological Journal of China Universities, v. 13, p. 463-473.